Mechanistic basis of the dynamic response of TWIK1 ionic selectivity to pH

Franck C. Chatelain[1,2], Nicolas Gilbert[1,2], Delphine Bichet[1,2], Annaïse Jauch[3], Sylvain Feliciangeli[1,2], Florian Lesage[1,2,*], Olivier Bignucolo[1,4]

[1] Université Côte d'Azur, Centre national de la recherche scientifique, Institut national de la santé et de la recherche médicale, Institut de pharmacologie moléculaire et cellulaire, 06560 Valbonne, France
[2] Laboratories of Excellence, Ion Channel Science and Therapeutics, 06560 Valbonne, France
[3] Immunodeficiency Laboratory, Department of Biomedicine, University of Basel and University Hospital of Basel, Switzerland.
[4] Swiss Institute of Bioinformatics, Basel, Switzerland
* Corresponding author, E-mail: lesage@ipmc.cnrs.fr

Short title: Residues underlying the pH-dependence of TWIK1 ionic selectivity

Abstract

At neutral pH, the TWIK1 channel is highly selective for K^+. When exposed to acidification, it becomes permeable to Na^+. This change occurs within minutes and is reversible. By combining pKa calculations, molecular dynamics (MD) simulations, mutagenesis and electrophysiology, we identified a network of residues involved in this unique property. MD simulations captured crucial features associated with channel gating and previously observed by cryogenic electron microscopy (cryo-EM) at pH7.4 and pH5, such as the pH-dependent orientation of the lateral side chain of the proton sensor His122 and the elongation of the entire pore structure upon acidification. Between the closed and open states of TWIK1 observed by cryo-EM, MD simulations show that the channel undergoes additional conformational changes between pH 7.5 to 6 that involves the His122, Glu235, Lys246 and Phe109 residues. A complex network of interactions surrounding the selectivity filter at high pH transforms into a simple set of stronger interactions at low pH. In particular, His122 protonated by acidification moves away from Lys246 and engages in a salt bridge with Glu235. In addition, stacking interactions between Phe109 and His122, which stabilize the selectivity filter in its K^+-selective state at high pH, disappear upon acidification. This causes dissociation of the Phe109 aromatic side chain from this network, ultimately leading to the Na^+-permeable conformation of the channel.

Introduction

TWIK1 belongs to the family of K^+ channels with two pore domains (K_{2P}). TWIK1 has distinctive features: it is expressed in many tissues, it is constitutively endocytosed from the plasma membrane to recycling endosomes, and its ionic selectivity depends on variations in extracellular or intra-endosomal pH. In particular, a decrease in pH from 7.4 to 6 induces a decrease in K^+ ion selectivity, allowing TWIK1 to conduct Na^+ ions [1, 2]. This change in ionic selectivity leads to a reduction in the net flow of positive charges, with the inflow of Na^+ opposing the outflow of K^+. This change in selectivity is slow and reversible [3, 4]. In endosomes with intravesicular acidic pH, Na^+-permeable TWIK1 could contribute to organelle acidification by helping to substitute Na^+ for H^+. At the cell surface, TWIK1 current could facilitate membrane hyperpolarization or depolarization, depending on its recycling rate between the plasma membrane and recycling endosomes [1, 2]. Gene inactivation of TWIK1 in pancreatic and renal cells leads to an increase of the resting membrane potential, indicating that, in these cells, it behaves as a depolarizing channel permeable to Na^+ [1, 2, 5]. Hypokalemia has also been shown to promote a shift in TWIK1 ionic selectivity

toward the Na^+-permeable state. This dynamic selectivity underlies the paradoxical depolarization of human cardiomyocytes during hypokalemia [1].

Active K_{2P} channels are dimer of subunits, each subunit containing two pore domains (P1 and P2) that contribute to the formation of the ionic pore. TWIK1 has unique residues in these domains that are involved in its ionic selectivity. We have shown that the T118I mutation in the P1 domain suppresses extracellular pH sensitivity and dynamic selectivity, producing a channel locked in the K^+-selective state[1]. We have also identified residues contributing to its sensitivity to pH: His122, which is the primary pH sensor, and Leu108 and Phe109, two pore helix residues. The H122N mutation abolishes TWIK1 sensitivity to acidification whereas the L108F/F109Y mutation produces a channel that is constitutively permeable to Na^+ [2]. Progressive acidification causes first a slight increase in TWIK1 current between pH7.5 to 6.5, then a decrease associated with a substantial change in ionic selectivity below pH6.5 [2]. The current produced by the H122K mutant, which mimics the protonated state of the His122 side chain upon acidification, is already maximal between pH7.5 to 7.0, but still exhibits the ionic selectivity change below pH6.5 [2] suggesting that His122 is not the only pH-sensitive structural element involved in this change. Previous studies have described the structures of TWIK1 in its open state at pH8 (24) and 7.4 (8), and in its close state at pH5 (8). However, how TWIK1 becomes permeable to Na^+ at pH6 has not yet been studied. To elucidate the molecular mechanism controlling the dynamic response of TWIK1 to pH, we used a comprehensive approach combining mutagenesis and electrophysiology experiments with pKa calculations and molecular dynamics (MD) simulations.

Results

A method to identify residues involved in the response of TWIK1 ionic selectivity to pH

Progressive acidification of the extracellular pH has sequential effects on TWIK1. First, channel activity increases between pH7.5 and pH6.5, then ionic selectivity changes at lower pH levels as shown by the shift of the reversal potential (**Fig. 1A)** (2). As observed with H122K (2), the H122R mutation that mimics the protonation of the His122 side chain leads to an increase in TWIK1 activity at high pH, without affecting the subsequent change in ionic selectivity at lower pH (**Fig. 1B**). To identify the residues involved in this selectivity change, we first focused on the area of the selectivity filter (**Fig. 1C** and **Fig. 2**). pKa calculations guided us in selecting residues to be titrated for the MD simulations (**Fig. 2A**) and the trajectories from these simulations were analyzed to unravel alterations within atomic networks (**Fig. 4 and Fig. S1**). Mutations of TWIK1 residues were then designed to test putative mechanisms within the limits of available natural amino acids. For example, replacing histidine with an asparagine gives comparable side-chain volumes and hydrophilicity while suppressing protonation at low pH. The next sections describe how interactions between His122, Lys246, Glu235, Phe109 and Ser106 (**Fig. 2C**) as well as Asp230 (**Fig. 2D**) respond to acidification. These descriptions provide an atomic-level overview of pH-induced responses for most of these key elements.

The Glu235-Lys246 interaction

Lys246 is located in the M4 membrane-spanning helix, while Glu235 is found in the extended, flexible loop connecting the SF2 and M4 domains (**Fig. 1C, Fig 2B-C** and **Fig. 4B**). This SF2-M4 loop, stabilized by a network of hydrogen bonds, is known to be important for the function of TREK and TASK K_{2P} channels [3, 4]. Like H122R, the TWIK1.E235Q mutant shows maximal channel activity at pH7.5, with no activation phase between 7.5 and 7.0 (**Fig. 3A**). Notably, this mutation has no effect on the change of ionic selectivity below pH6, as shown by the shift in reversal potential between pH7.5 and pH6 (ΔE_{Rev} = 17.31 ± 2.63 mV) (**Fig. 3A** middle panel and **Table 1**). The ionic selectivity of the K246Q mutant is almost identical from pH7.5 to 6.0, resembling TWIK1 at pH7.5. However, below pH7 current amplitude of the K246Q mutant increases and remains high at pH6, in contrast to TWIK1 (**Fig. 3B**). These results suggest that Glu235 is involved in the activation phase but not in the selectivity change, while Lys246 is involved in this change but not in channel activation. We then tested double mutations. The E235Q-K246Q mutation that disrupts the strong

electrostatic interactions between these two residues eliminates both channel activation and ionic selectivity change (**Fig. 3C**). E_{Rev} is stable over the entire tested pH range, showing that ionic selectivity is unaffected (**Fig. 3C**, central panel). To confirm the importance of electrostatic interactions in this region, the two residues were swapped in the TWIK1.E235K-K246E mutant. This channel shows a pH response comparable to that of TWIK1 with a change in ionic selectivity at low pH, with ΔE_{Rev} becoming significantly different below pH6 (ΔE_{rev} =17.19 ± 3.93, **Table 1**) (**Fig. 3D**). These results demonstrate that Glu235 and Lys246 are involved in the pH sensitivity of TWIK1.

The His122-Glu235-Lys246 triad

To understand how His122 interacts with Glu235 and Lys246, we performed MD simulations. Unbiased simulations were conducted at pH7.4 and pH6.0. Protonation states of the titratable residue were initialized on the basis of their calculated pKa values, generating approximately 12.0 µs of simulation distributed across 36 distinct protein trajectories, 18 at each pH value. Additional simulations with the TWIK1.H122N mutant were carried out. These simulations encompassed 16 independent protein trajectories, again 8 at each pH value, for a total of 2.4 µs. The protonation pattern was identical, with the exception of residue 122. The region examined within the protein is illustrated in **Fig. 4A**, while **Fig. 4B** shows representative snapshots of typical interactions under the 4 conditions studied. Our data suggest that acidification gives rise to salt bridge linking His122 and Glu235, and that the dynamics of this salt bridge may contribute to pH sensitivity (**Fig. 4E).** At pH7.4, this salt bridge is broken within a few tens of ns (**Fig. S1**). This pairwise analysis does not reveal a pH effect on the distance between His122 and Lys246 in TWIK1, whereas this distance is slightly increased by acidification in TWIK1.H122N (**Fig. 4E**). Due to the low value of its calculated pKa (**Fig. 2A**), Lys246 was deprotonated and neutral at both pHs, whereas Glu235 remained unprotonated and negatively charged. However, the distance between these residues decreases significantly upon acidification (**Fig. 4E** and **Fig. S1**). As their protonation states are identical at both pH values, another interaction is required to explain this observation. The distance between Glu235 and Lys246 is not affected by pH in TWIK1.H122N, suggesting that protonation of His122 is necessary to induce this distance decrease. We have generated two-dimensional maps depicting distance distributions to analyze how distances between these three residues respond to pH and mutation. The frequency of occurrences is color-coded using a gradient from violet to yellow, with shades from light green to yellow indicating regions of highest occurrence density (**Fig. 5**). We began by examining the Glu235-Lys246-His122 triad and analyzing distance maps. Specifically, we plotted Glu235-Lys246 distances along the X-axis and residue122-Glu235 distances along the Y-axis (**Fig. 5A**). At high pH, three distinct regions emerge for TWIK1. The first graph from the left contains a greenish region labeled "a," indicating states where Glu235 interacts with Lys246 (approximately 4 Å along the X-axis), while its interaction with His122 remains relatively weak. This greenish region corresponds to a distance between His122 and Glu235 ranging from 6.5 to 10 Å. A yellow region labeled "b" characterizes a short distance between His122 and Glu235 (around 5 Å) coupled with a substantial Glu235-Lys246 distance along the X-axis (8 Å). Notably, no data points correspond to simultaneous Glu235-Lys246 and His122-Glu235 interactions. This observation suggests that at pH7.4, Glu235 engages either with Lys246 or with His122, but not both simultaneously. In the third major conformation visited at this pH, Glu235 interacts with neither His122 nor Lys246 (“c”). At acidic pH (**Fig. 5A,** second graph from the left), this complex pattern disappears: almost all conformations converge on a region typical of a salt bridge connecting His122 and Glu235. Intriguingly, a small subset of conformations appears in which all three residues simultaneously interact (« d »), a conformation that is totally absent at high pH. While the low pH-induced salt bridge between Glu235 and His122 is detectable in **Fig. 4E** and **Fig. S1**, its precise co-occurrence with a distance of approximately 8 Å between Glu235 and Lys246 (region « e » in **Fig. 5A**) could not be guessed. This remarkable collapse of a multifaceted histogram to a singular state upon acidification is not seen in the simulations in which Asn122 replaces His122 (**Fig. 5A**, plots on the right). In **Fig. 5B** we represented this triad of residues by plotting the Glu235-Lys246 distances on the X-axis and the His122-Lys246 distances on the Y-axis. These graphs reveal that two populations of fairly short identical His122-Lys246 distances overlap in TWIK1 at neutral pH (**Fig. 5B**, left). As above, for TWIK1 and TWIK1.H122N, the

distribution converges toward a simpler representation at low pH, characterized by an increase in the distance between His122 and Lys246.

The dissociation of Phe109 from His122 at low pH contributes to the loss of ionic selectivity

We have previously demonstrated the importance of residue Phe109 in the change of selectivity associated with pH (2). In the crystal structure resolved at pH8 (24) and the cryogenic electron microscopy (Cryo-EM) structure at pH7.4 (8), the side chains of residues Phe109, His122, Gly235, Lys246 and Ser106 form a pocket (**Fig. 2C** and **Fig. 4**). The distance between Phe109 and Lys246 is not affected by pH (**Fig. 4E**) whereas the distance between His122 and Phe109 is significantly increased at low pH, as shown in **Fig. 6**, X-axes. The two-dimensional plots of the distances between Phe109-His122 and His122-Glu235 side chains suggest that at high pH, most of the conformations corresponding to a large His122-Glu235 distance (Y-axis) coincide with His122 lying~ 6Å from Phe109 (X-axis), likely forming aromatic stacking interactions (**Fig. 6A, left**). Once again, the complex distribution at neutral pH reduces to a much simpler pattern at low pH, where most conformations correspond to the aforementioned His122-Glu235 salt bridge. This salt bridge is incongruent with concurrent aromatic stacking interactions, as many conformations converge into a solitary population with distances between aromatic rings spanning around 11 Å (**Fig. 6A**, second plot from the left). The H122N variant does not show such a marked effect (**Fig. 6A**, third and fourth plots). These data suggest that, at high pH, His122, which is oriented at almost 90 degrees to the major axis of the protein, favours aromatic staking interactions with Phe109, whereas the reorientation of its protonated form at low pH, coinciding with its attraction by Glu235, disrupts aromatic interactions with Phe109. The hydrophobic nature of Phe109 prevents it from following the upward movement of the protonated His122, while it can still make contact with Lys246, forming staking interactions with the hydrophobic methylene groups of the lysine side chain [5]. Consequently, the distance between Lys246 and His122 increases under low pH conditions, in line with our observations (**Fig. 4E**, **Fig. 5B** and **Fig. 6B**). From a mechanical point of view, the release of Lys246 and Phe109, rendering this large hydrophobic residue available for other functions at the level of the central cavity, would contribute to the decrease in ion selectivity. This mechanism relies on the hydrophobic nature of phenylalanine. A tyrosine at this position could have less impact, as it could maintain weak interactions with His122, even in its protonated state. This is supported by the lack of pH sensitivity of the F109Y mutant (**Fig. S2A-D**). TWIK1 and the related K_{2P} channel TASK3 have a histidine at analogous positions (His122 and His98, respectively), whereas TASK3 has a tyrosine at position 85 instead of Phe109 in TWIK1 (**Fig. 1A**) [6, 7]. Currents generated by the Y85F mutant of TASK3 were tested at pH7.5 and pH6. In contrast to TASK3, the TASK3.Y85F shows a shift in reversal potential similar to that of TWIK1, confirming the role of Phe109 hydrophobicity in ionic selectivity change upon acidification (**Fig. S3A-C**). We evaluated another difference between TWIK1 and TASK3 in the degree of hydrophobicity close to the pH sensor. In the upper part of the first pore-helix domain of TWIK1, the side chain of Ser106 points towards His122 (**Fig. 2C)**, whereas in TASK3, a glycine (Gly82) occupies the equivalent position (**Fig. 1A**). Whereas the S106G mutation in TWIK1 reduces the impact of acidification on ionic selectivity (ΔERev = 7.88 ± 2 mV vs. 22.37 ± 1.56 for TWIK1, **Table 1**, **Fig. S2E**), the G82S mutation in TASK3 is marked by an increase in current inhibition associated with a much more pronounced shift in reversal potential (**Fig. S3A-B**), again confirming the importance of a hydrophilic residue at this position (106 in TWIK1) for the sensitivity of ionic selectivity to pH.

At low pH, Asp230 stabilizes interaction between the two subunits in the TWIK1 dimer

Asp230 has a calculated pKa of around 6 **(Fig. 2A**). Its replacement by an asparagine in the D230N mutant produces a Na^+-permeable channel at pH7.5 (**Fig. S4A**). The proximity between the residue Asp230 of one subunit and the residue Lys131 of the adjacent subunit in the crystal structure resolved at pH8.0 suggests the formation of a salt bridge (**Fig. 2B** and **2D).** This salt bridge would be disrupted by acidification and protonation of Asp230 favoring the Na^+-permeable state as observed with the TWIK.D230N mutant. However, replacing Lys131 with glutamine, a neutral residue of similar size and hydrophilicity does not suppress pH sensitivity, although the shift in reversal potential is less than in TWIK1 (TWIK1.K131Q mutant, **Fig. S4B-D**). These results underline the importance of these two residues, but rule out the existence of a salt bridge at high pH. Furthermore, MD simulations suggest that such a salt bridge between Asp230 of one

subunit and Lys131 of another subunit forms essentially at low pH (**Fig. 4E**) and in the WT channel. They also indicate that the distance between the carboxylic acid of Asp230 of one subunit and the imidazole of His122 of an adjacent subunit decreases significantly upon acidification and His122 protonation (**Fig. 4E**). The distance converges within 50ns in both TWIK1 and TWIK1.H122N (**Fig. S1**). The same trend was observed for the distance between Asp230 of one subunit and Glu235 of the adjacent subunit. These data suggest that upon acidification, Asp230 stabilizes interactions between the two subunits in the TWIK1 dimer.

Low pH promotes stronger interactions between His122 and the lower part of the CAP

The model of the membrane-inserted TWIK1 protein used for MD simulations was built from the 2012 structure identified by PDB accession code 3UKM (24). We compared the structures generated by MD simulation with those obtained more recently by cryo-EM at pH7.4 and 5 (8). In the cryo-EM structures, the orientation of His122 with respect to the main axis of the protein decreases significantly upon extracellular acidification [8]. For each frame, the protein was oriented along its major axis and the angle formed by the major axis and a line joining the Cα atom and the side chain of residue 122 was calculated. On average, the orientation of His122 relative to the major axis of the protein decreases from ~80 to ~50 degrees upon acidification. Interestingly, no response is observed with asparagine in the TWIK.H122N mutant, which remains at ~90 degrees at both pH values (**Fig. 4C**). Overall, probability histograms of the angle for Asn122 support unimodal distributions. In simpler terms, Asn122 rarely adopts a low-angle conformation, its distributions at both pH values being almost indistinguishable. Conversely, His122 exhibits a pronounced preference for a high-angle orientation at pH7.4 and a low-angle orientation at pH6. Notably, the simulations effectively replicated the behaviors inferred from the cryo-EM structures.

In terms of long-range conformational changes, the low pH structure is several Å longer than the high pH structure, mainly due to rearrangements of the helical CAP and transmembrane helices. To check whether long-range conformational changes are observable in the simulated structures, we selected the Cα atoms of two residues spanning the entire protein structure: His67 in the apex of the CAP, and Arg171 in the intracellular loop connecting TM2 and TM3. We compared the distance between them under the 4 conditions. These Cα atoms are shown in **Fig. 2B**. This sampling was sufficient to observe statistically significant long-range responses, as illustrated in **Fig. 4D**, which shows that the channel exposed to low pH elongates significantly by 2 to 3Å. This response is also observed with the TWIK1.H122N mutant, which was ~ 2Å longer in the trajectories corresponding to low pH conditions. A further consequence of His122 repositioning during acidification is a displacement of residues in contact with His122. This is illustrated by the reduced distance between the side chains of His122 and Ser86 under low pH conditions (**Fig. 4E**). While the centers of mass of their functional group are separated by around 10 Å at neutral pH, they move closer together by 6 Å at low pH. This movement closely reflects the high (13 Å) and low pH (9 Å) distances between these groups recorded in cryo-EM structures (8). A comparable decrease in distance upon acidification was also observed for Asn87 and Gly89. These distances were studied to highlight interactions between His122 and the lower segment of the CAP. Our results indicate that at low pH, His122 engages more frequently with residues of the Extracellular CAP helix 2 (EC2). This behavior is absent in the H122N mutant, confirming the idea that changes in pH have no impact on Asn122 orientation (**Fig. 4C** and **Fig. 4E**).

Discussion

This study reveals unique features in the TWIK1 pore that underly its response to pH. Acidification of the extracellular medium from pH7.5 to pH7 causes protonation of His122 and an increase in K^+ current. Then, for pH below 6.5, a second step involving residues located in the pore region leads to a change of ionic selectivity. We had already identified some of the residues involved in the dynamic selectivity of TWIK1, notably Thr118 in the SF1 signature sequence, and His122 and Phe109, located respectively at the extracellular exit of the selectivity filter and in the SF1 pore-helix. Here, we identify Glu235 and Lys246 whose interactions with the main proton sensor His122 are crucial for the ionic selectivity change. Both residues are situated in the SF2-M4 loop, at the interface between the P1 and M4 regions. Their side chains

occupy the same space as His122, Phe109 and the polar residue Ser106, and interact with them. MD simulation suggests that during the protonation process, His122 ceases to interact with Phe109 and, in a movement of its side chain toward the CAP, establishes a stable salt bridge with Glu235 in the SF2-M4 loop. This pair transforms into a triad with Lys246 located in the M4 helix, which approaches Glu235, forming rare conformations in which all three residues interact. Glu235 and Lys246 have low calculated pKa values, so that the interaction mentioned here describe a case in which three residues share a proton. These data suggest that, at pH values slightly lower than the ones considered here (pH<6), Glu235 and Lys246 would share an additional proton. In this case, the triple interaction could strengthens, restraining the two M4 helices closer to the pore, in a mechanism reminiscent to the previously described KvAP potassium channel deactivation [9]. The replacement of Glu235 by a non-titratable residue in the E235Q mutation or its interaction with protonated His122 seems to place the channel in a state of maximal activity at a pH value above pH6.5. This state of maximal activity persists at pH values higher than 6.0, for K246E and E235Q-K346Q mutants, all three conditions preventing the formation of the interaction Lys246-Glu235-His122 mentioned above. The importance of this channel region has already been highlighted in the description of K^+-dependent gating of the TREK1 K_{2P} channel. In a study combining data from crystallography, electrophysiology and MD simulations, the authors showed that under low K^+ conditions, the selectivity filter undergoes a significant reorganization of its architecture at the S1 and S2 sites as well as a large movement of the SF2-M4 loop that results in the inhibition of ion conduction. The binding of a specific TREK1 activator in the P1-M4 interface of this channel limits the movement of the SF2-M4 loop and stabilizes the channel in an open conformation [4]. A recent study of the pH–dependent gating of the alkaline-activated TALK1 channel also highlighted this region as essential for channel inactivation [10]. TALK1 contains an arginine residue in place of Lys246 in TWIK1, and its activation occurs at a remarkable high pH [11]. The authors found that Arg233 of TALK1 acts as a main proton sensor, its deprotonation triggering a sequence of allosteric changes that stabilize the S1 site of the filter in a conductive state. Notably, activation curves of TALK1 and R233K mutant show an acidic shift of about 3 pH units in the latter case, which mimics Lys246 of TWIK1. Compared with the TREK1 and TALK1 channels, TWIK1 is unique in that acidification induces a conformational rearrangement of its pore region that first alters its ion selectivity before leading to channel closure.

Previously reported TWIK1 structures have all been obtained under high K^+ concentrations, showing an open state at pH7.4 or 8 and a close state at pH5. Several studies have shown that K^+ ion concentration significantly affects the gating, permeability and selectivity of K^+ channels [4, 12-14]. Our results show that when K^+ concentration is close to the physiological level (2mM), the regulation of TWIK1 by extracellular pH is much more complex than a simple switch from a conducting to a non-conducting state. Among the information provided by these structures, the most relevant is certainly the significant displacement of the two residues His122 and Asp230. The disorganization of the pore K^+-binding S0 and S1 at acidic pH, which probably results from the reorientation of these two residues but also from the weakening of the interaction forces located behind the selectivity filter, is reminiscent of the pore of the NaK channel whose conversion to a K^+-selective channel depends on the presence of the four binding sites S1 to S4 capable of coordinating K^+ ions [15]. It is now generally admitted that, with the exception of TASK1 and TASK2 channels for which an additional inner gate has been described [16, 17], the selectivity filter of the K_{2P} channels is the main site of regulation of their activity, a regulation known as C-type gating in the other families of K^+ channels [3]. TWIK1 also exhibits C-type gating. However, TWIK1 has outstanding features at the pore level. With two non-conserved residues in the P domains and multiple residues sensitive to pH in crucial positions, TWIK1 responds in a unique way to proton modulation. In most K_{2P} channels the action of pH is monophasic, a decrease of the activity for TREK1, TASK1/2/3 and TALK1/2 channels and an activation for TREK2 [11]. TWIK1 has a biphasic response: its activity augments when exposed to a modest pH drop, then its ionic selectivity changes for stronger acidifications. Our results do not allow us to conclude on the level of conduction of TWIK1 at pH lower than pH6, the pore could be in a non-conductive state as proposed by the cryo-EM at pH5.5 and 150 mM K^+.

TWIK1 is conductive and non-selective at pH6 and predominantly distributed in recycling endosomes suggesting that TWIK1 could play a dual role as a classical K^+-selective channel at the plasma membrane, and

as a K^+ and Na^+-permeable channel in endosomes. Its recycling rate between the surface and the endosomes may therefore modulate its selectivity and its influence on the resting membrane potential. A pharmacological compound acting on the selectivity filter of TWIK1 to stabilize the channel in either the K^+-selective or Na^+-permeable form would be a useful tool to decipher its physiological roles. Another interesting result is that this unique property of TWIK1 can be transferred to TASK3 by introducing only a few residues typical of TWIK1. In TASK3, Y85F and G82S mutant show a response to pH similar to that of TWIK1. TASK3 is known to be involved in cell proliferation and carcinogenesis [18, 19]. Interestingly, a TASK3.G82S variant has been described in the COSMIC database, as a somatic mutation found in adenocarcinoma (COSM3897140, COSV57284824, ICGC (STAD-US): Gastric Adenocarcinoma - TCGA, US). This mutation was found in gastric tissues in which the channel exposed to acidic pH should be permeable to K^+ and Na^+. It would be certainly interesting to study how this selectivity change of TASK3 affects cancer development.

Material and Methods

Mutagenesis and oocyte expression. TWIK1 and its mutants were cloned into the HindIII–XhoI sites of a derivative of pGEM vector. All channels used in this study were designed from the active form of TWIK1 in which the internalization and inhibitory intracellular basic motifs were mutated (mutations K274E, I293A, and I294A) [11]. Site-directed mutagenesis was performed based on PCR of the full-length plasmid by using Pfu Turbo DNA polymerase (Stratagene). The entire cDNA was sequenced. TWIK1 and TWIK1 mutant cDNAs were linearized at the AflII restriction site, and capped cRNA were synthesized by using the AmpliCap-Max™ T7 High Yield Message Maker Kit (CellScript™). The animals used for oocyte collection were treated and sacrificed in accordance with procedures filed with and accepted by the French Ministry of Agriculture under authorization #14012-20180302144339 v3. Stage V–VI *Xenopus laevis* oocytes were collected, injected with 5–10 ng of each cRNA, and maintained at 18 °C in ND96 solution (96 mM NaCl, 2 mM KCl, 1 mM MgCl2, 5 mM Hepes, pH7.4).

Electrophysiology. Oocytes were used 1–3 days after injection. Macroscopic currents were recorded with two-electrode voltage clamp (TEV 200 amplifier; Dagan). Electrodes were filled with 3 M KCl and had a resistance of 0.5–2MΩ. A small chamber with a perfusion system was used to change extracellular solutions and was connected to a ground by a 3M KCl agarose bridge. All constructs were recorded in ND96 at designated pH adjusted with NaOH. For pH-sensitivity experiments, all recordings were done in standard ND96 solution, adjusting pH with NaOH to values of 6 to 7.5. For every pH, the solution was buffered with 5 mM MES and 5 mM HEPES, and the pH was adjusted with NaOH 2N. Currents were evoked from a −80-mV holding potential followed by a 300-ms ramp from −120 to +60 mV. All recordings were performed at 20 °C. Stimulation, data acquisition, and analysis were performed using pClamp software (Molecular Devices). The graphs, statistical analyses and figures related to the electrophysiology have been realized on the GraphPad Prism software. Statistical significance was determined by using unpaired Student's t test and indicated as follows: *P < 0.05; **P < 0.01; ***P < 0.001. ****<0.0001

Computational section. The inter-residue distance calculations reported in Table 1 and the 3D-structure representations S1 and S2 have been realised on PyMOL software from the crystal structure of TWIK1 (PDB ID: 3UKM, chains A and B). The 3D-structure representations reported in Figures 4 and 5 were realised with VMD [20]. Other structural features reported were calculated using a combination of GROMACS [21] tools and Python scripts. Where appropriate, multifactorial ANOVA were conducted.

pKa calculations. pKa calculations are often performed uniquely on the available structure, so that conformational changes occurring upon proton binding or unbinding cannot be estimated. Also, changes in protonation states of a given residue affect its electrostatic environment, which may further modify the probability of a neighbouring residue to bind or release a proton. These issues are recognized, and it is tried to solve them implicitly through rearrangement of charges as a function of the dielectric constants of the

protein and the solvent. Yet, these strategies were shown to fail when facing complicated proteins [22, 23]. In this work, we aimed at overcoming these limitations by designing a new strategy that involves several successive short MD simulations harbouring progressive protonation states until convergence. The atomic model of the TWIK1 channel was initially built on the basis of the 3UKM crystal structure [24], which is assumed to correspond to an open state, and completed for short missing loops using SWISS-MODEL [25]. The model was inserted in a 1-palmitoyl-2-oleoyl-sn-glycerol-3-phosphocholine (POPC) bilayer (≈ 230 molecules) and solvated (≈ 55000 water molecules) at 0.15 M KCl. A first 10 ns long simulation was conducted, and frames extracted at 2 ns interval for pKa calculations using a solver of the Poisson-Boltzmann (PB) equation. The length of the simulation was chosen to be sufficiently long to induce some relaxation of the biomolecules while staying short enough to avoid large conformational changes of the protein. The CHARMM module PBEQ (Poisson-Boltzmann equilibrium) was used because of its accuracy and versatility. For each frame, the pKa were then calculated as done previously [26]. Briefly, after the first MD simulation and pKa estimation, the protonation state of titratable residues was updated as a function of the desired pH. A second MD simulation was then conducted, starting from the same initial configuration, but with these residues protonated. Such successive rounds "MD simulation + pKa calculation" were conducted until no more residues had to be modified. All glutamate, aspartate, lysine and histidine of TWIK1 residues were submitted to this process. Using this approach, we computed the pKa values for titratable residues, focus on residues exhibiting values between 8 and 4 (**Fig. 2A**), many of which form a ring encircling the extracellular aspect of the pore (**Fig. 2B**). A decreasing trend of pKa values emerged from the pore's core to its exterior. Subsequently, unbiased MD simulations were conducted to replicate systems at pH7.4 and pH6.0. Titratable residue protonation states were initialized based on their pKa values, generating approximately 12.0 µs of simulation distributed across 36 distinct protein trajectories. Notably, due to the pH insensitivity of the H122N mutant [2, 8] (**Fig. 1B**), additional simulations of this variant were executed. These simulations encompassed 16 independent protein trajectories, accumulating a total of 2.4 µs. The identical protonation pattern was maintained, with the exception of residue 122.

Here we report the protonation states of the residues located close to the studied area, comprising all titratable residues located within 12Å from the Cα atom of residue 122. In this surrounding, His122, Glu45, Glu49 and Asp230 were protonated at low pH only, Glu235 was left negatively charged in all cases, whereas Lys246 and Lys131 were deprotonated in all cases.

Molecular Dynamics simulations. We constructed models of the channel based on the crystal structure with PDB code 3UKM, which was prepared at a pH greater than 7.4 and is believed to represent an open conformation. These models were protonated to simulate either pH6.0 or pH7.4 and were embedded in a double bilayer system, following a previously established method [9]. It's important to note that this system was different from the one used for the pKas calculations. In each extracellular-facing leaflet of the bilayer, there were 105 molecules of 1-palmitoyl-2-oleoyl-sn-glycerol-3-phosphocholine (POPC) and 10 of 1-palmitoyl-2-oleoylphosphatidylethanolamine (POPE). To partially recreate the negative charge inside biological membranes, the cytoplasmic-facing leaflet contained 10 negatively charged dimyristoylphosphatidylglycerol (DMPG) molecules and 105 POPC molecules only. These numbers were chosen to ensure that both leaflets had a comparable surface area, considering the structure of the channel. After solubilisation in 150 mmol·L-1 KCl and neutralisation, a typical simulation box contained ∼ 243'000 atoms. For the wild-type (WT) sequence, we performed a total of 18 trajectories at each pH, resulting in a cumulative simulation time of 6.3 µs at pH 7.4 and 5.6 µs at pH6.0. A similar procedure was followed for the H122N mutant, except that in this case, we conducted four simulations, each lasting 300 ns, at each pH value. Therefore, the total trajectory time dedicated to the H122N mutant was 2.4 µs. The all-atom MD simulations were performed with the CHARMM36 force field, using the GROMACS package version 2021.5. The TIP3P water model was used [27]. Bond and angle lengths involving hydrogen atoms were constrained using the LINCS algorithm allowing an integration time step of 2 fs. Short-range electrostatics were cut off at 1.2 nm. Van der Waals interactions were calculated explicitly up to 10 Å, beyond which a switch function was used to smoothly switch off the interactions to reach zero at 12 Å. Long-range electrostatic interactions were calculated by the PME algorithm [28]. The protein, lipids, and water/ions were coupled separately to a

temperature bath with the Nose-Hoover method with a time constant of 1.0 ps [29, 30]. The system pressure was kept constant by semi-isotropic Parrinello-Rahman coupling to a reference value of 1 bar as implemented in the GROMACS suite. GROMACS and in-house Python scripts were used to analyse the data. The first 50 ns were discarded in all calculations involving angles and distances.

Acknowledgements

This work was funded by the Agence Nationale de la Recherche (grants ANR-11-LABX-0015-01 and ANR ANR-22-CE14-0048-01), by the Fondation pour la Recherche Médicale (équipe labellisée FRM 2020), and the Swiss National Supercomputing Center (CSCS) under the project IDs s968, s1037, s1099 and s1223. We thank Solène Gibaud for excellent technical help, and S. Bernèche and D. Minor for useful comments on the manuscript.

Author contributions

F.C.C., N.G., D.B., A.J. and O.B. performed the experimental work. S.F., F.L. and all the other authors contributed to experience design, data analysis and manuscript writing.

Competing interest

The authors declare no competing interest.

Data availability

All data to support the conclusions are available in the main text or the Supplementary Information. All other data are available from the corresponding author upon request.

Figure legends

Figure 1

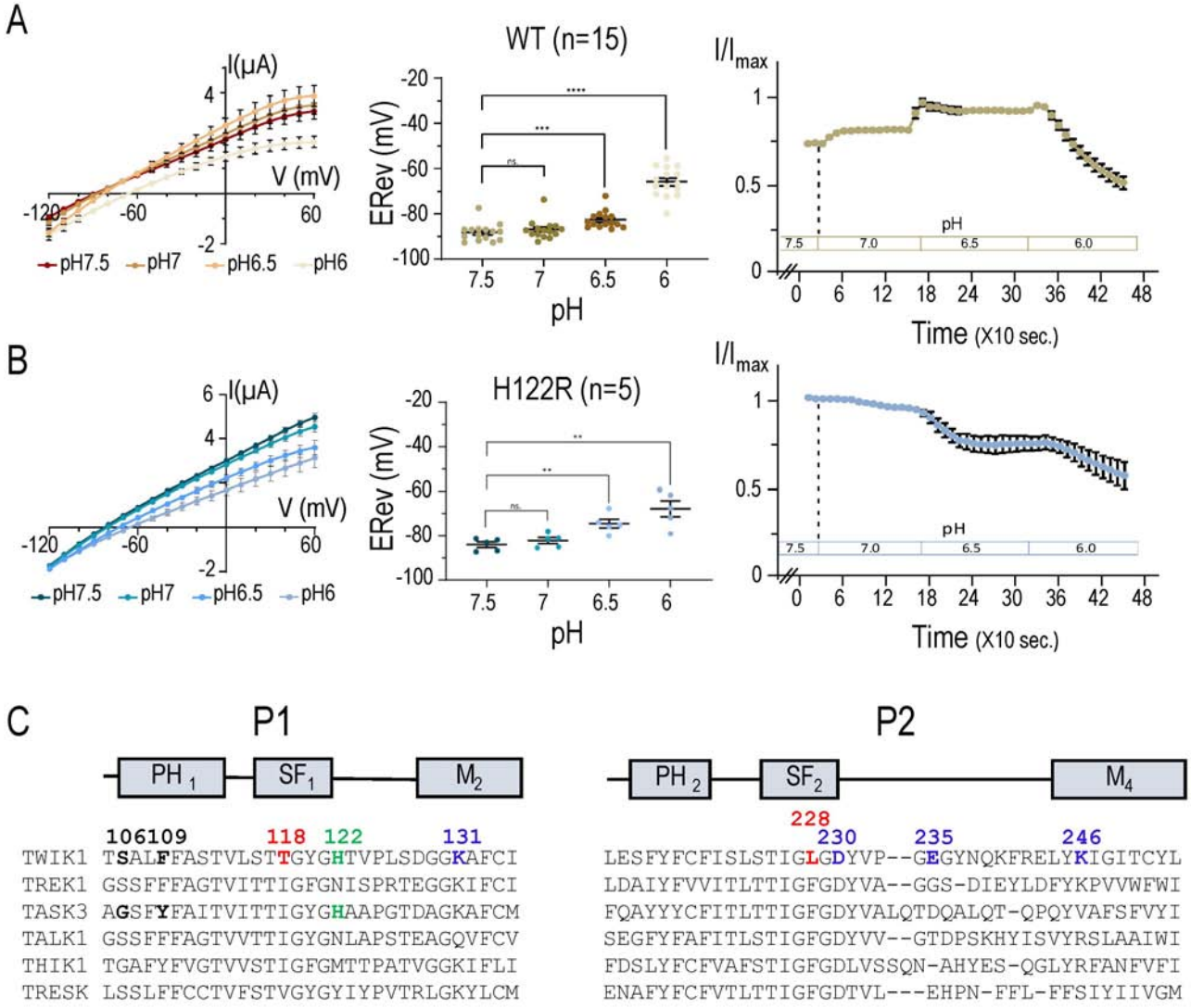

Figure 1. **Residues affecting the pH-dependent selectivity of TWIK1.** (**A**, **B**) TWIK1 (**A**) and TWIK1.H122R (**B**) currents recorded in *Xenopus* oocytes at pH7.5, pH7, pH6.5 and pH6. In brackets the number of oocytes recorded. After stabilization of the currents at pH7.5, voltage ramps were applied from -120 mV to +60 mV every ten seconds. pH was changed every 150 sec starting from pH7.5 to pH6. Left panels: I/V curves recorded during the stabilized currents at different pH. Extracted from the voltage ramp recorded at each pH before changing to the next one. Middle panels: reversal potentials (E_{Rev}) measured during these stabilized currents. Right panels: Kinetics of the current variations as a function of the pH, measured at 0 mV every 10 seconds. pH changes are indicated. All data are presented as mean ± SEM; ns, non-significant; *, $p < 0.05$; **, $p < 0.01$; ***, $p < 0.001$; ****, $p < 0.0001$. (**C**) Amino acid sequence alignment of human K_{2P} channels. Key residues are shown in bold or color. PH, pore helix domain; SF, selectivity filter domain; M, membrane-spanning helix.

Figure 2

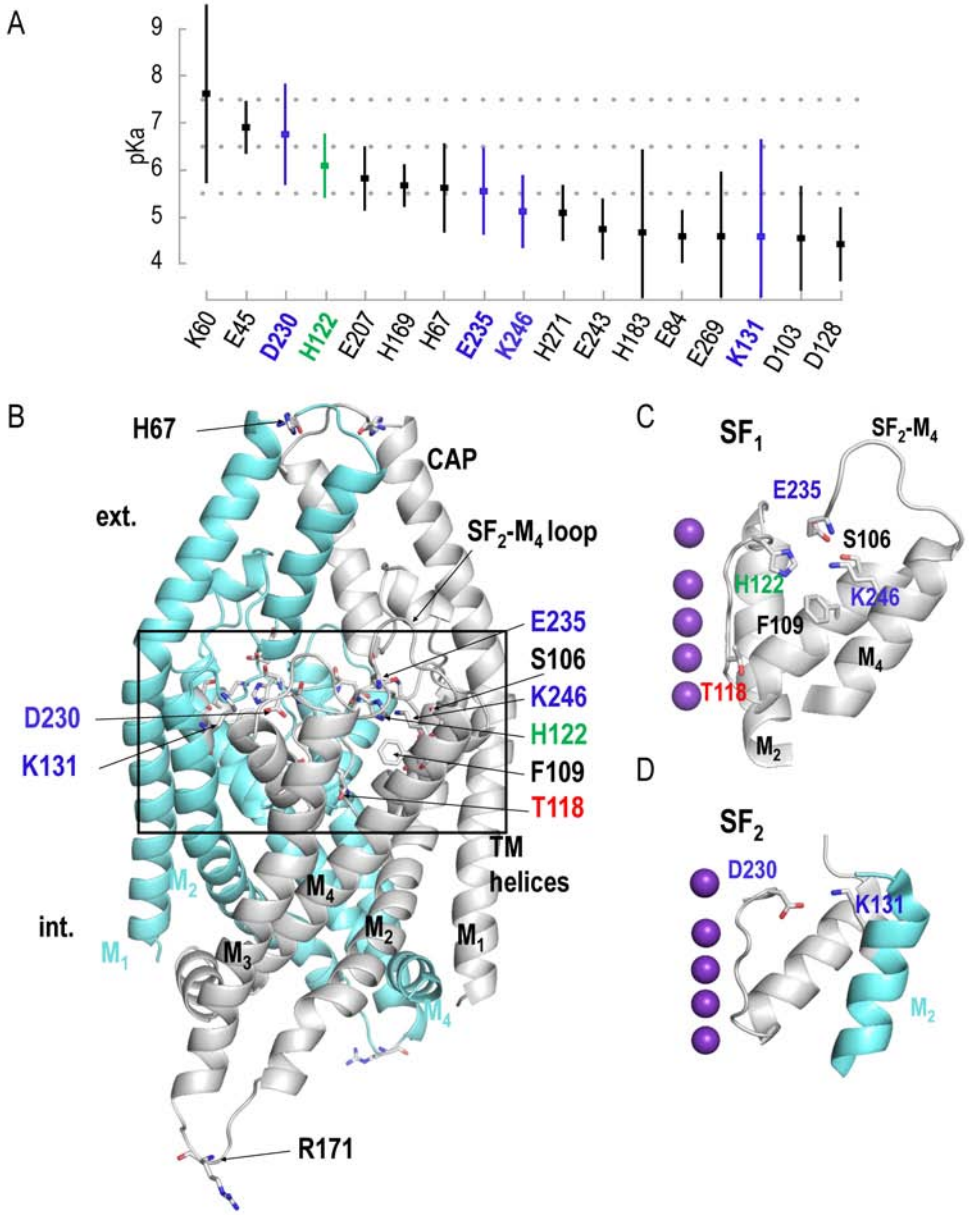

Figure 2. **Titratable residues in TWIK1.** (**A**) Calculated pKas are presented in decreasing order for the values between 8.0 and 4.0 (means ± standard deviations, n = 12). (**B**) Molecular representation of TWIK1, based on the crystal structure (PDB code 3UKM). The two TWIK1 subunits are shown in two different colors: subunit 1 in grey and subunit 2 in cyan. The side chains of residues S106, F109, H122, D230, E235, K246 of the same subunit converge towards the same region buried behind the selectivity filter 1 (SF1). The side chain of residue D230 of one subunit points in the direction of that of residue K131 of the neighbouring subunit behind the selectivity filter 2 (SF2). The residue Arg171 has been built using SWISSMODEL into the PDB structure in order to appear in the structure. (**C**, **D**) Regions behind the selectivity filter 1 (**C**) and selectivity filter 2 (**D**). To facilitate visualization of the molecular organization of each pore domain, we have shown on these views neither the CAP region nor the parts of the structure masking these regions. In purple the K^+ ions in their respective S sites in the crystal structure.

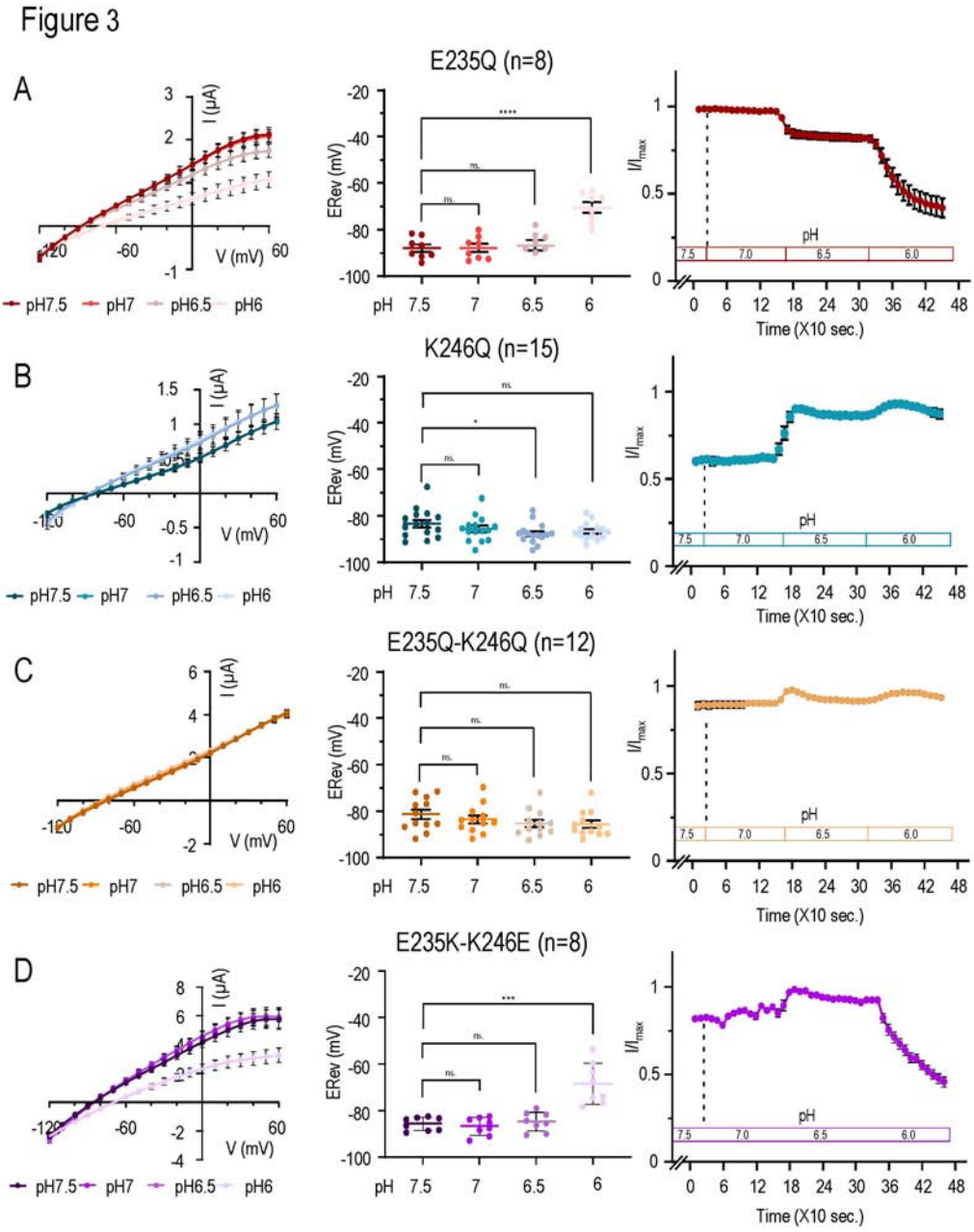

Figure 3. **pH response of currents produced by TWIK1-E235Q, K246Q, E235Q-K246Q and E235K-K246E mutants.** (**A-D**) Currents of E235Q (**A**), K246Q (**B**), E235Q-K246Q (**C**) and E235K-K246E (**D**), recorded in *Xenopus* oocytes at pH7.5, pH7, pH6.5 and pH6. In brackets the number of oocytes recorded. After stabilization of the currents at pH7.5, voltage ramps were applied from -120 mV to +60 mV every ten seconds. pH was changed every 150 sec. starting from pH7.5 to pH6. Left panels: I/V curves recorded during the stabilized currents at different pHs extracted from the voltage ramp recorded at each pH before changing to the next one. Middle panels: reversal potentials (E_{Rev}) measured during these stabilized currents. Right panels: Kinetics of the current variations as a function of the pH, measured at 0 mV every 10 seconds. pH changes are indicated. All data are presented as mean ± SEM; ns, non-significant; *, $p < 0.05$; **, $p < 0.01$; ***, $p < 0.001$; ****, $p < 0.0001$.

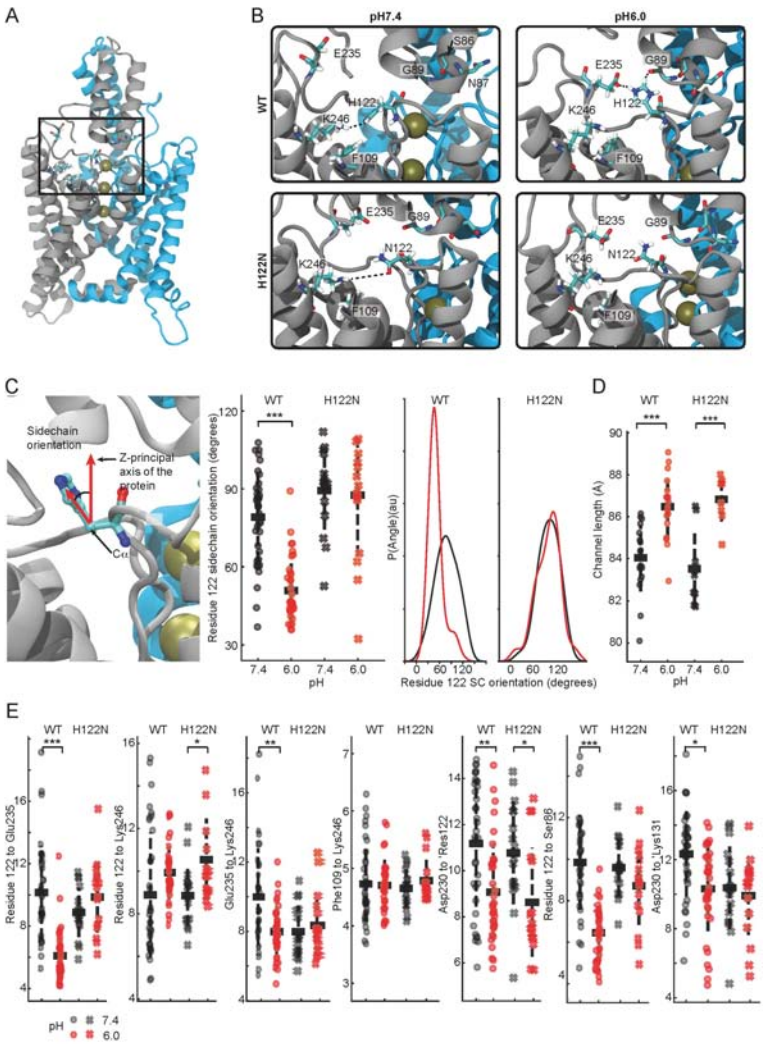

Figure 4

Figure 4. **MD simulations.** (**A**) Molecular representation of TWIK1. The subunits are colored in blue and grey, and the studied region is indicated. The residues discussed in the text are shown as sticks. (**B**) Magnifications of the investigated region showing typical conformations adopted by the WT model at pH6.0 (upper left) and at pH7.4 (upper right) and by the H122N variant at pH6.0 (lower left) and at pH7.4 (lower right). Interactions are indicated by dotted lines. (**C**) Left: Determination of the residue 122 orientation in respect to the channel principal axis. The vertical red arrow indicates a vector parallel to the protein principal axis. The second vector joins the Cα atom of residue 122 with the centre-of-mass of selected side chain pairs of atoms, which are ND1 and NE2 in the case of His and OD1 and ND2 in the case of Asn. Middle: Orientation of residue 122 as a function of the pH and the identity of the residue. Each point represents the average of the values taken in each subunit over an independent 300-600 ns long simulation. Means, standard deviation and the results of a t-test are indicated. Right: Histograms of residue 122 orientation, fitted using the non-parametric Kernel density estimation function of the Python Pandas suite. All four distributions are unimodal. (**D**) Distance between the Cα atoms of His67 and Arg171, used as proxies for the length of the channel along its principal axis, are shown as a function of the pH and the identity of residue 122. For this analysis the appropriate replicate for the statistics is the whole channel, i.e., the values of two subunits were pooled. (**E**) Distances between the centres-of-mass of side chain heavy atoms of pairs of residues as a function of both the pH and the identity of residue 122. Residues labels of the neighbouring subunit are preceded by the prefix '. Each point represents the average of the values taken in each subunit over an independent 300-600 ns long simulation. The results of statistical analyses are presented as follows: *, $p < 0.05$; **, $p<0.01$, ***, $p<0.001$. For simplification, P values below 0.001 are not further identified, but are considered as $p<0.001$.

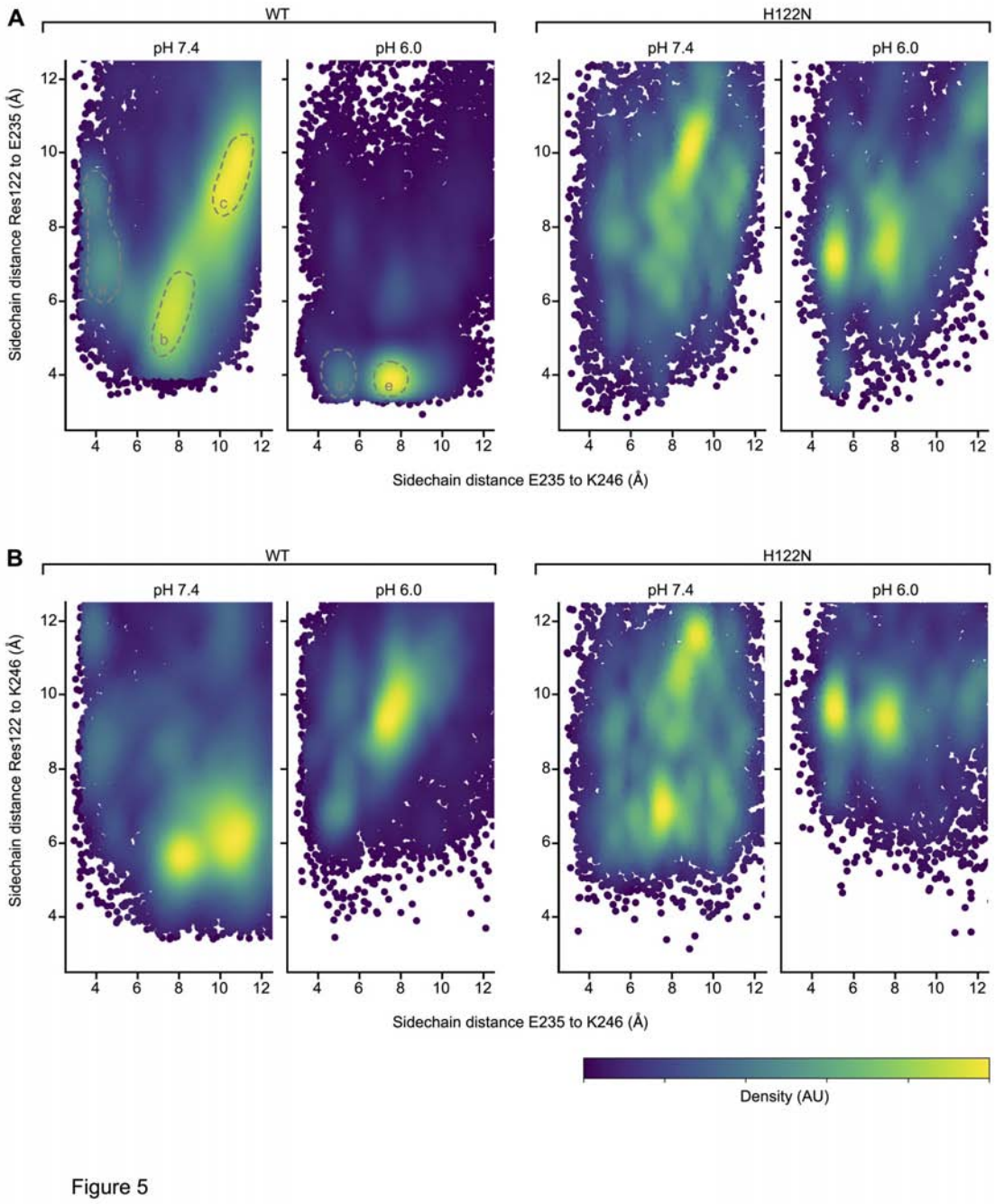

Figure 5. **Distance landscape representations of the interactions involving residue 122, Glu235 and Lys246** (**A**) Distances between the side chains of Glu235 and Lys246 (X-axis) and between residue 122 and Glu235 (Y-axis) under four different conditions from left to right: TWK1 at pH7.4, TWIK1 at pH6.0, TWIK1.H122N at pH7.4, and TWIK1.H122N at pH6.0. The frequencies of occurrences are shown, yellow indicating the highest densities. The populated areas discussed in the text are indicated. The pH6.0 plot indicates that the His122-Glu235 salt bridge, identified in Fig. 5E, occurs essentially when the Glu235 and Lys246 are at ~ 8Å from each other. (**B**) Similar distance maps with the Y-axis corresponding to the distances between residue 122 and Lys246.

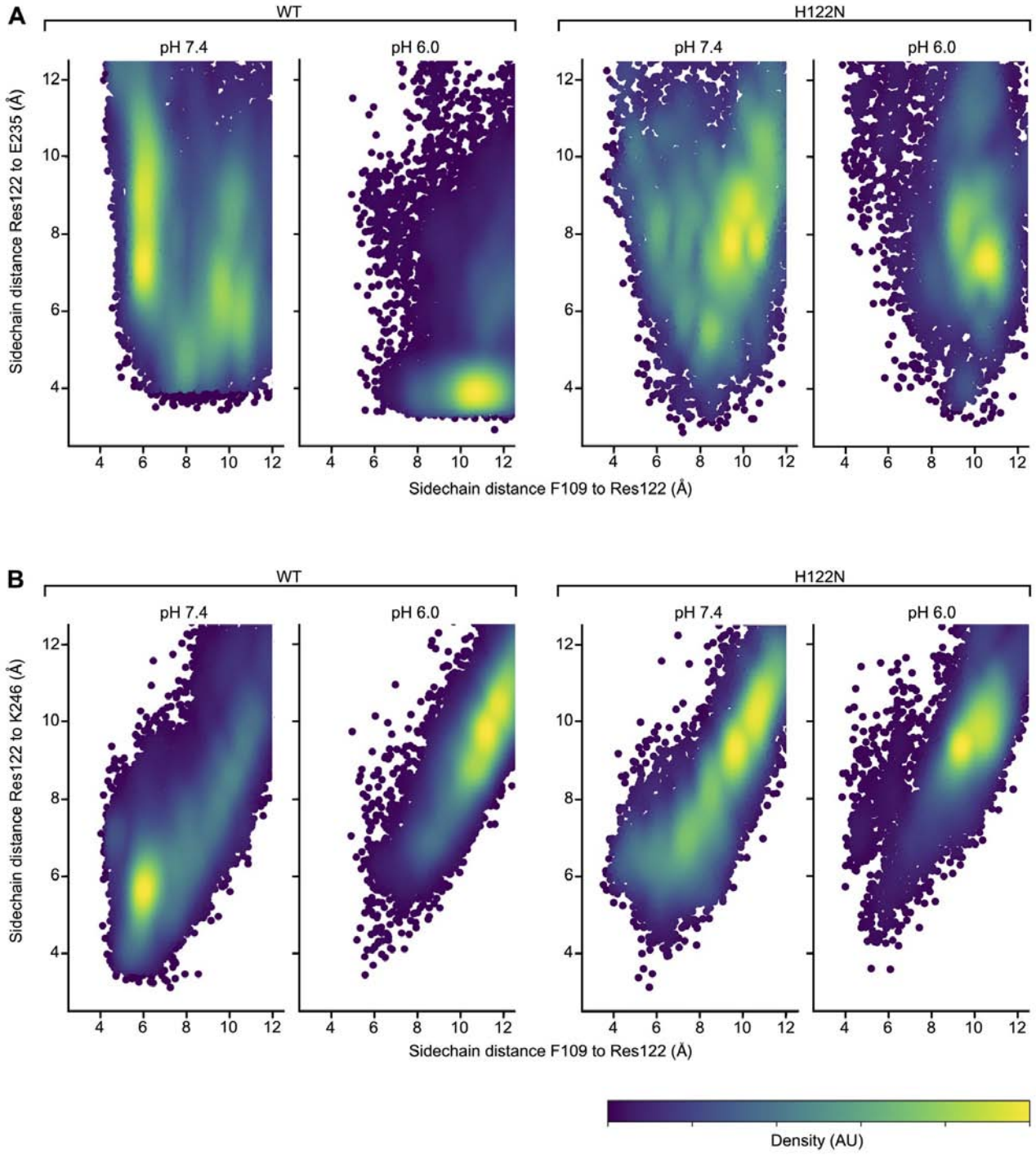

Figure 6

Figure 6. **Distance landscape representations of the interactions involving residue 122, Phe109, Glu235 and Lys246.** (**A**) Distances between the side chains of residue 122 and Phe246 (X-axis) and between residue 122 and Glu235 (Y-axis) under four different conditions from left to right: WT sequence and pH7.4, WT sequence and pH6.0, H122N variant and pH7.4, H122N variant and pH6.0. The frequencies of occurrences are shown, with yellow indicating the highest densities. (**B**) Similar distance maps, whereas the Y-axis corresponds to the distances between residue 122 and Lys246.

Table 1

Construct	Current at $I_{0\ mV}$ (mA)				Erev (mV)				ΔERev (mV) between pH7.5 and pH6
	pH7.5	pH7.0	pH6.5	pH6	pH7.5	pH7.0	pH6.5	pH6	
TWIK1 (n=15)	2.15 ± 0.23	2.36 ± 0.26	2.69 ± 0.29	1.47 ± 0.17	-88.21 ± 0.99	-86.87 ± 1.092	-82.64 ± 0.98	-65.83 ± 1.69	22.37 ± 1.56
T118I (n=6)	3.20 ± 0.86	3.54 ± 1.06	2.87 ± 1.14	4.30 ± 1.26	-79.67 ± 3.2	-82.67 ± 3.13	-83.67 ± 2.43	-84.17 ± 2.13	-4.5 ± 1.64
L228F (n=14)	1.27 ± 0.46	N/A	N/A	1.20 ± 0.40	-93.35 ± 2.17	N/A	N/A	-93.93 ± 2.21	-0.58 ± 1.15
F109Y (n=8)	0.19 ± 0.02	N/A	N/A	0.13 ± 0.01	-57.9 ± 4.25	N/A	N/A	-50.22 ± 6.26	6.87 ± 2.84
H122N (n=6)	1.09 ± 0.31	1.08 ± 0.35	1.034 ± 0.31	0.987 ± 0.30	-67 ± 1.79	-67.5 ± 0.95	-66.25 ± 0.62	-64.75 ± 0.75	2.25 ± 2.17
D230N (n=6)	0.32 ± 0.10	0.36 ± 0.11	0.34 ± 0.11	0.33 ± 0.11	-20.01 ± 3.21	-18.3 ± 2.69	-16.08 ± 2.17	-14.79 ± 2.12	5.22 ± 1.55
K131Q (n=14)	4.54 ± 0.45	5.21 ± 0.52	5.766 ± 0.56	3.36 ± 0.32	-88.47 ± 0.94	-88.45 ± 1.00	-87.66 ± 0.98	-81.47 ± 1.55	6.99 ± 1.13
S106G (n=6)	1.42 ± 0.18	1.52 ± 0.19	1.59 ± 0.24	1.57 ± 0.29	-87 ± 1.5	-87.29 ± 1.62	-82.88 ± 1.78	-79.12 ± 2.41	7.88 ± 2.00
H122R (n=6)	3.0 ± 0. 05	2.83 ± 0.07	2.21 ± 0.15	1.68 ± 0.24	-84.00 ± 1.27	-82.16 ± 1.37	-74.51 ± 1.99	-67.8 ± 3.54	16.14 ± 3.44
E235Q (n=8)	1.43 ± 0.13	1.41 ± 0.13	1.19 ± 0.12	0.63 ± 0.14	-87.75 ± 1.59	-87.72 ± 1.74	-86.63 ± 2.22	-70.44 ± 2.27	17.31 ± 2.63
K246Q (n=17)	0.51 ± 0.06	0.51 ± 0.06	0.73 ± 0.01	0.77 ± 0.01	-83.21 ± 1.60	-85.60 ± 1.38	-87.54 ± 1.12	-86.61 ± 0.93	-3.39 ± 1.13
E235Q-K246Q (n=12)	2.20 ± 0.26	2.22 ± 0.26	2.28 ± 0.28	2.33 ± 0.28	-81.17 ± 2.01	-83.27 ± 1.74	-84.97 ± 1.62	-85.32 ± 1.59	-4.15 ± 1.81
E235K (n=10)	1.96 ± 0.14	1.30 ± 0.14	0.79 ± 0.11	0.342 ± 0.03	-84.58 ± 1.09	-76.27 ± 1.32	-59.58 ± 2.30	-32.59 ± 2.38	51.98 ± 2.42
K246E (n=11)	0.88 ± 0.10	1.03 ± 0.11	0.96 ± 0.10	0.53 ± 0.05	-86.65 ± 0.87	-72.73 ± 1.01	58.81 ± 1.13	-44.14 ± 1.34	42.51 ± 1.66
E235K-K246E (n=8)	4.18 ± 0.37	4.49 ± 0.41	4.59 ± 0.37	2.32 ± 0.33	-85.58 ± 1.00	-86.64 ± 1.35	-84.68 ± 1.44	-68.38 ± 3.11	17.19 ± 3.93

Table 1: **Key values from electrophysiological recordings of TWIK1 mutants.** In brackets the units of measurement (µA for the currents and mV for the imposed potential) or the number of *Xenopus* oocytes recorded per construction. ΔERev reflects the shift of the reversal potentials between pH7.5 and pH6. N/A stands for non-available.

References

1. Ma, L., X. Zhang, and H. Chen, *TWIK-1 two-pore domain potassium channels change ion selectivity and conduct inward leak sodium currents in hypokalemia.* Sci Signal, 2011. **4**(176): p. ra37.
2. Chatelain, F.C., et al., *TWIK1, a unique background channel with variable ion selectivity.* Proc Natl Acad Sci U S A, 2012. **109**(14): p. 5499-504.
3. Natale, A.M., P.E. Deal, and D.L. Minor, Jr., *Structural Insights into the Mechanisms and Pharmacology of K2P Potassium Channels.* J Mol Biol, 2021. **433**(17): p. 166995.
4. Lolicato, M., et al., *K2P channel C-type gating involves asymmetric selectivity filter order-disorder transitions.* Sci Adv, 2020. **6**(44).
5. Garst, A.D., et al., *Crystal structure of the lysine riboswitch regulatory mRNA element.* J Biol Chem, 2008. **283**(33): p. 22347-51.
6. Morton, M.J., et al., *Determinants of pH sensing in the two-pore domain K(+) channels TASK-1 and -2.* Pflugers Arch, 2003. **445**(5): p. 577-83.
7. Rajan, S., et al., *TASK-3, a novel tandem pore domain acid-sensitive K+ channel. An extracellular histiding as pH sensor.* J Biol Chem, 2000. **275**(22): p. 16650-7.
8. Turney, T.S., V. Li, and S.G. Brohawn, *Structural Basis for pH-gating of the K(+) channel TWIK1 at the selectivity filter.* Nat Commun, 2022. **13**(1): p. 3232.
9. Bignucolo, O. and S. Berneche, *The Voltage-Dependent Deactivation of the KvAP Channel Involves the Breakage of Its S4 Helix.* Front Mol Biosci, 2020. **7**: p. 162.
10. Tsai, W.H., et al., *Allosteric coupling between transmembrane segment 4 and the selectivity filter of TALK1 potassium channels regulates their gating by extracellular pH.* J Biol Chem, 2022. **298**(6): p. 101998.
11. Lesage, F. and J. Barhanin, *Molecular physiology of pH-sensitive background K(2P) channels.* Physiology (Bethesda), 2011. **26**(6): p. 424-37.
12. Kiss, L., et al., *The interaction of Na+ and K+ in voltage-gated potassium channels. Evidence for cation binding sites of different affinity.* J Gen Physiol, 1998. **111**(2): p. 195-206.
13. Tsukamoto, H., et al., *Structural properties determining low K(+) affinity of the selectivity filter in the TWIK1 K(+) channel.* J Biol Chem, 2018. **293**(18): p. 6969-6984.
14. Nematian-Ardestani, E., et al., *Selectivity filter instability dominates the low intrinsic activity of the TWIK-1 K2P K(+) channel.* J Biol Chem, 2020. **295**(2): p. 610-618.
15. Derebe, M.G., et al., *Tuning the ion selectivity of tetrameric cation channels by changing the number of ion binding sites.* Proc Natl Acad Sci U S A, 2011. **108**(2): p. 598-602.
16. Rodstrom, K.E.J., et al., *A lower X-gate in TASK channels traps inhibitors within the vestibule.* Nature, 2020. **582**(7812): p. 443-447.
17. Li, B., R.A. Rietmeijer, and S.G. Brohawn, *Structural basis for pH gating of the two-pore domain K(+) channel TASK2.* Nature, 2020. **586**(7829): p. 457-462.
18. Zuniga, R., et al., *TASK-3 Downregulation Triggers Cellular Senescence and Growth Inhibition in Breast Cancer Cell Lines.* Int J Mol Sci, 2018. **19**(4).
19. Pei, L., et al., *Oncogenic potential of TASK3 (Kcnk9) depends on K+ channel function.* Proc Natl Acad Sci U S A, 2003. **100**(13): p. 7803-7.
20. Humphrey, W., A. Dalke, and K. Schulten, *VMD: visual molecular dynamics.* J Mol Graph, 1996. **14**(1): p. 33-8, 27-8.
21. Van Der Spoel, D., et al., *GROMACS: fast, flexible, and free.* J Comput Chem, 2005. **26**(16): p. 1701-18.
22. Langsetmo, K., et al., *Linkage of thioredoxin stability to titration of ionizable groups with perturbed pKa.* Biochemistry, 1991. **30**(30): p. 7609-14.
23. Dillet, V., H.J. Dyson, and D. Bashford, *Calculations of electrostatic interactions and pKas in the active site of Escherichia coli thioredoxin.* Biochemistry, 1998. **37**(28): p. 10298-306.

24. Miller, A.N. and S.B. Long, *Crystal structure of the human two-pore domain potassium channel K2P1.* Science, 2012. **335**(6067): p. 432-6.
25. Biasini, M., et al., *SWISS-MODEL: modelling protein tertiary and quaternary structure using evolutionary information.* Nucleic Acids Res, 2014. **42**(Web Server issue): p. W252-8.
26. Bignucolo, O., et al., *Galvani Offset Potential and Constant-pH Simulations of Membrane Proteins.* J Phys Chem B, 2022. **126**(36): p. 6868-6877.
27. Jorgensen, W.L., et al., *Comparison of simple potential functions for simulating liquid water.* The Journal of Chemical Physics, 1983. **79**(2): p. 926-935.
28. Essmann, U., et al., *A smooth particle mesh Ewald method.* The Journal of Chemical Physics, 1995. **103**(19): p. 8577-8593.
29. Nosé, S., *A molecular dynamics method for simulations in the canonical ensemble.* Molecular Physics, 2006. **52**(2): p. 255-268.
30. Hoover, W.G., *Canonical dynamics: Equilibrium phase-space distributions.* Phys Rev A Gen Phys, 1985. **31**(3): p. 1695-1697.